3D Morphometric Analysis of Human Fetal Cerebellar Development

Julia A. Scott,
Biomedical Image Computing Group, Departments of Pediatrics, Bioengineering, and Radiology, University of Washington, Seattle, WA 98195, USA

Kia S. Hamzelou,
Department of Molecular and Cell Biology, University of California, Berkeley, Berkeley, CA 94720, USA

Vidya Rajagopalan,
Biomedical Image Computing Group, Departments of Pediatrics, Bioengineering, and Radiology, University of Washington, Seattle, WA 98195, USA

Piotr A. Habas,
Biomedical Image Computing Group, Departments of Pediatrics, Bioengineering, and Radiology, University of Washington, Seattle, WA 98195, USA

Kio Kim,
Biomedical Image Computing Group, Departments of Pediatrics, Bioengineering, and Radiology, University of Washington, Seattle, WA 98195, USA

A. James Barkovich,
Department of Radiology and Biomedical Imaging, University of California, San Francisco, San Francisco, CA 94131, USA

Orit A. Glenn, and
Department of Radiology and Biomedical Imaging, University of California, San Francisco, San Francisco, CA 94131, USA

Colin Studholme
Biomedical Image Computing Group, Division of Neonatology, Departments of Pediatrics, Bioengineering and Radiology, University of Washington, Seattle, WA 98195, USA

Julia A. Scott: jascott1@uw.edu

Abstract

To date, growth of the human fetal cerebellum has been estimated primarily from linear measurements from ultrasound and 2D magnetic resonance imaging (MRI). In this study, we use 3D analytical methods to develop normative growth trajectories for the cerebellum in utero. We measured cerebellar volume, linear dimensions, and local surface curvature from 3D reconstructed MRI of the human fetal brain ($N = 46$). We found that cerebellar volume increased approximately 7-fold from 20 to 31 gestational weeks. The better fit of the exponential curve ($R^2 = 0.96$) compared to the linear curve ($R^2 = 0.92$) indicated acceleration in growth. Within-subject cerebellar and cerebral volumes were highly correlated ($R^2 = 0.94$), though the cerebellar percentage of total brain volume increased from approximately 2.4% to 3.7% ($R^2 = 0.63$). Right

and left hemispheric volumes did not significantly differ. Transcerebellar diameter, vermal height, and vermal anterior to posterior diameter increased significantly at constant rates. From the local curvature analysis, we found that expansion along the inferior and superior aspects of the hemispheres resulted in decreased convexity, which is likely due to the physical constraints of the dura surrounding the cerebellum and the adjacent brainstem. The paired decrease in convexity along the inferior vermis and increased convexity of the medial hemisphere represents development of the paravermian fissure, which becomes more visible during this period. In this 3D morphometric analysis of the human fetal cerebellum, we have shown that cerebellar growth is accelerating at a greater pace than the cerebrum and described how cerebellar growth impacts the shape of the structure.

Keywords

Cerebellum; Fetal MRI; Brain development; Posterior fossa; Vermis

Introduction

In the later half of gestation, the human brain grows and increases in structural complexity at a more rapid rate than in any other period of development [1–4]. The cerebellar cortex is undergoing extensive foliation leading to accelerating increases in surface area [5, 6]. Contributing to this morphological development are the processes of neurogenesis and establishment and elaboration of cerebellar fiber pathways, which begin around 13 gestational weeks (GW) and continue until early in the second year after birth [7]. The major events from 20 to 30 GW include differentiation of Purkinje cells, maximal proliferation in the external granular layer, and migration of precursor cells from the external granule cell layer [6].

Cerebellar expansion is linked with the proliferation of the external granular layer and migration of precursor cells to the internal granular layer. Migration from the ventricular zone to the deep cerebellar nuclei is reaching completion near 30 GW. Although myelination of the brainstem is detectable after 24 GW, myelination within the cerebellum and of cerebellar peduncles occurs after 32 GW [8]. While the major fissures are established by 20 GW, further foliation and secondary fissures are formed after this time [9–11].

While these micro- and macroscopic developments have been well established from postmortem and histological studies, growth patterns of the human cerebellum in the living brain have been limited to ultrasonography measurements, 2D fetal magnetic resonance imaging (MRI), and 3D MRI of premature neonates. Estimations of cerebellum or vermis size are routinely carried out by ultrasonography, and normative growth trajectories have been established [12, 13]. In one study, cerebellar volume was estimated from multiplanar measurements of 3D ultrasound [14] and in another from 3D reconstructed fetal MRI [15]. 2D fetal MRI has also been used to replicate ultrasonography findings [11, 16]. Volumetric studies of the healthy and injured premature brain by 3D MRI provide a close approximation of in utero fetal cerebellar development [17, 18]; however, direct measurement from the fetus in utero would be more representative of normal development.

Recent advances in fetal MRI processing [19] have led to the 3D morphometric analysis of the cerebrum in the healthy brain in utero [20–22]. In this study, we have applied volumetry and local curvature analyses to the cerebellum in 3D reconstructed MRIs of living, healthy human fetuses. Understanding the development of the cerebellum is of considerable clinical value since the cerebellum is especially vulnerable to direct and indirect injury in premature birth [6, 18, 23].

Materials and Methods

Subjects and Fetal Image Acquisition

Data used in the present paper were acquired from an imaging study that was approved by our local Institutional Review Board and complies with National Institutes of Health human subject guidelines. Exclusion criteria were multiple gestation pregnancy, chromosomal abnormality diagnosed prenatally or postnatally, and brain abnormalities on fetal MRI. Mothers provided informed consent for use of fetal scans for research purposes. The mothers were referred for fetal MRI either to better assess questionable findings on prenatal ultrasound ($N = 7$) or due to a prior abnormal pregnancy ($N = 10$) or to volunteer for the study ($N = 23$) (Table 1). Mothers enrolled in the studies ranged in age from 19 to 41 years (mean, 34 years). Mean age did not differ between maternal volunteers and patients ($T = 0.5$, $p = 0.62$). Maternal age did not correlate with gestational age at MRI ($R^2 = 0.0086$, $p = 0.57$). Of the study scans that met image acquisition criteria for image analysis (TR = 3,000–9,000 ms; slice thickness ≈ 3 mm; sufficient number of stacks; fetal motion less than 15 mm translation and 30° of rotation between slices), we selected 46 clinical scans of 40 fetuses (19 males, 21 females) at gestational ages ranging from 20.57 to 31.14 GW, estimated by last menstrual period (Fig. 1).

All of the fetal MRI used in this study were read as normal by a fetal neuroradiologist (O.A.G.). Neither the mother nor fetus were sedated, and the mother was free breathing for the scan duration of 20 to 45 min. Clinical MR imaging was performed on a 1.5-T scanner (GE Healthcare, Milwaukee, WI, USA) using an eight-channel torso phased-array coil. Multiple stacks of single-shot fast spin-echo T2w slice images (in-plane pixel size ≈ 0.5 × 0.5 mm; slice thickness ≈ 3 mm, no gap) were planned in the approximately axial, sagittal, and coronal planes with respect to the fetal brain. The underlying spatial resolution of the original 2D multi-slice data was between 0.8 and 1.0 mm, prior to clinically requested re-gridding to between 0.4 and 0.5 mm in-plane pixel size for radiological inspection on clinical picture archiving and communication system. All slice images were acquired in an interleaved manner to reduce saturation of spins in adjacent slices. The MR sequence parameters (TR = 3,000–9,000 ms; TE = 91 ms) were originally designed for clinical scans and were not adjusted for tissue segmentation in this study. From these clinical acquisitions, one to four stacks were selected in each plane for 3D image reconstruction. To account and correct for spontaneous fetal movement during scanning, all image slices in the slice stacks of a subject were registered using the slice intersection motion correction technique [24] and reconstructed into 3D volumes with isotropic voxel dimensions of 0.5 mm.

Volumetric Analysis of the Cerebellum

The cerebellum was manually delineated using RView image analysis software (http://rview.colin-studholme.net). The sagittal plane was used for segmentation with concurrent review of the coronal and axial planes. Segmentation proceeded lateral to medial in the right and left hemispheres (Fig. 2a), and the midsagittal slice was used to delineate vermal area (Fig. 2b). All sagittal slices lateral to the midsagittal slice were included in the hemisphere tissue label such that the hemispheric volumes included part of the vermis. The lateral hemispheres were distinguished by a clear perimeter of extracerebellar CSF. The dorsal boundary often abutted the tentorium cerebelli, in which case the boundary was defined with the lower edge of the tentorium rather than CSF. Progressing medially, the cerebellar peduncles and brainstem became visible anterior to the cerebellum. These structures were delineated from the cerebellum by a diagonal contour from the flexure at inferior–posterior lobe and the peduncles to the anterior aspect of the anterior lobe. In the vermal region, the fourth ventricle formed the anterior boundary and surrounding CSF or the tentorium cerebelli formed the remaining boundaries.

Linear Dimensions of the Cerebellum

The transcerebellar diameter (TCD), vermal height (VH), and vermal anterior–posterior diameter (VAP) were manually measured on the cerebellum segmentations. TCD was defined as the maximum distance from the right to left hemispheres in the coronal plane (Fig. 2c). On the midsagittal vermal slice, VH and VAP were calculated. VH was the greatest inferior to superior distance, and VAP was the distance from the apex of the fourth ventricle to the posterior extent of the vermis (Fig. 2d).

Growth Trajectory Estimations

Linear, quadratic, and exponential estimations of right, left, vermal, and total cerebellar growth were tested. Right and left hemispheric volumes were compared by a paired T test. The growth rates of cerebellar volume and cerebral volume [20] were compared by a linear regression of the ratio of cerebellar volume to the sum of cerebellar and cerebral volumes. The linear correlation between cerebellar and cerebral volumes was also calculated.

Linear models were used to estimate growth rates for TCD, VH, and VAP. Then the predictive values of the linear dimensions for cerebellar volume and vermal area were tested. An exponential model for cerebellar volume was calculated with TCD as the only parameter. Similarly, a linear model was calculated for vermal area with VH and VAP as parameters.

Registration and Local Curvature Analysis

The resulting label map of each subject was smoothed at two levels using a 2.0-mm full width at half-maximum (FWHM) Gaussian kernel first then a 1.5-mm FWHM Gaussian kernel (Fig. 3 a, b). To account for the overall growth of the cerebellum, the maps were linearly scaled to a single subject and then tessellated into triangular meshes using a topology-preserving marching cubes algorithm [25] (Fig. 3 c). The local geometry of each surface was quantified using mean surface curvature H [26] calculated at each mesh vertex. Unlike other shape indices, mean curvature provides a physically interpretable measure of surface geometry—positive values of H express the convexity of a region, whereas negative values of H indicate the level of local concavity.

For the purpose of temporal modeling of shape changes, spatial mappings were defined between subject anatomies with different gestational ages and a common coordinate system (Fig. 3 d). Smoothed tissue maps of all subjects were co-aligned using a template-free approach [21, 27]. This registration procedure estimated a minimum deformation anatomy of the group and spatial mappings from this reference anatomy to each individual subject. Based on these mappings, measurements of local surface curvature of each subject were mapped onto a population-average surface obtained by tessellation of the reference anatomy. Age-related changes in local curvature at each vertex υ on the reference surface were represented using a linear model $H(\upsilon, t) = \beta_0(\upsilon) + \beta_1(\upsilon)t$ with coefficients found through least squares fitting to measurements of curvature mapped from subjects with different gestational ages t. Statistical significance of the $\beta_1(\upsilon)$ term was assessed using permutation testing [28] (Fig. 3 e).

Results

Cerebellar Growth Trajectories

The cerebellum increased in volume by approximately 7-fold from 20 to 31 GW (Fig. 4). The rate of growth steadily increased and therefore the quadratic and exponential models better fit the growth trajectory than a linear model by comparison of adjusted R^2 values (Table 2). Similar accelerating trajectories were estimated for the right and left cerebellar

volumes (Fig. 4; Table 2) with no significant difference in volume by hemisphere ($p =$ 0.9076). Age-related change in vermal area was best fit by a linear model (Fig. 4; Table 2) and increased by approximately 3.5-fold.

Cerebellar and cerebral volumes were strongly correlated ($R^2 = 0.94$), such that at equivalent gestational ages, a larger cerebellum was associated with a larger cerebrum. The cerebellar ratio of total brain volume increased significantly from 2.4% to 3.7% over this period of development ($R^2 = 0.63$). Therefore, the cerebellum was increasing in size relatively faster than the cerebrum [20]. This is also supported by the lower relative increase in cerebral volume over the same period (4.5-fold).

The cerebellar diameters (TCD, VH, and VAP) significantly increased linearly (Table 2). The relative increase in each diameter measurement from 20 to 31 GW was approximately 2-fold (Fig. 5). TCD (in centimeters) was a strong predictor of cerebellar volume ($R^2 = 0.96$) in an exponential relationship ($y = 1.15e^{16.69TCD}$). VH and VAP (in centimeters) were also significant predictors for vermal area ($y = 0.09VH + 0.08VAP - 0.08$) ($R^2 = 0.93$).

Age-Related Cerebellar Curvature Changes

The surface morphometry of the cerebellum underwent expansive change from 20 to 31 GW (Fig. 6). The most striking significant changes in curvature were detected in the inferior paravermian region. The inferior surface of the vermis increased in concavity (Fig. 6 c), while the adjacent inferior–posterior lobe of the hemispheres increased in convexity (Fig. 6 b). In addition to changes in curvature along the inferior surface, the apex of the vermis also increased in convexity with development (Fig. 6 b). Lastly, the aspect of the anterior lobe facing the brainstem increased in concavity (Fig. 6 b).

In the right hemisphere, there was a small area of increased convexity along the medial surface bordering the vermis (Fig. 6 b). The only other significant increase in convexity occurred along the lateral aspect of the right hemisphere (not shown). However, the left hemisphere also showed positive change in convexity, but did not pass significance after multiple comparisons correction.

Bilaterally, the inferior, superior, and anterior surfaces of the lateral hemispheres decreased in convexity (Fig. 6 c). This pattern was not specific to a particular cerebellar lobe, but to much of the superior surface and hemispheric regions that had the greatest curvature at younger gestational age.

Discussion

We report calculated growth trajectories for cerebellar volume and acceleration in cerebellar expansion that was not revealed by diameter measurements from 20 to 31 GW. Moreover, we show the predictive relationship between traditional diameter measurements and cerebellar volume and vermal area, underscoring the clinical value of these efficient measurements. Beyond scalar growth, the cerebellum changes in shape as tissue is added in specific local patterns.

Comparison to Diameter and Volume Studies

The diameter values reported here closely match published values from MRI studies of larger populations. The linear models predicted TCD within 3 mm and VH and VAP within 2 mm of comparable gestational age groups in independent studies [11, 16, 29]. Generally, measurements on 3D reconstructed images were smaller than past MRI studies, and the percent difference in mean values decreased with age to as Cerebellum low as 3%. Though growth rates reported here and in other MRI studies were similar to those based on

ultrasonography measurements of diameter, values from past MRI studies were smaller on average than ultrasonography-based measurements of the vermis [12] or transcerebellar diameter [13]. Despite the absolute difference in measurements across studies, cerebellar and vermal diameters are still highly correlated with the estimation of gestational age [30], and differences may be due to the particular appearance of the cerebellum in each imaging modality.

The cerebellar volumes derived from our manual segmentation of T2-weighted 3D reconstructed images were consistently smaller by 0.5 to 2 cm^3 than 3D ultrasound estimations of volume from 21 to 31 GW [14, 31]. Relative to our results, this corresponds to volumes 33% to 41% greater, on average. Like the diameter measurements, the appearance of cerebellar features used in manual segmentation inherently differ in volumetric ultrasonography and may result in reliably greater estimations in size.

Our volumetric results were in close agreement with the only other fetal cerebellar 3D reconstructed MRI study. In particular, our values fell within the 95% confidence interval for cerebellar volumes between 21 and 31 GW [15]. Notably, Hatab et al. [15] only used scans that were subjectively selected for low motion artifact and did not correct for motion in the image reconstruction process, which was done for the images used in our study. In comparison to the only 2D T2-weighted MRI study with comparable age range, our volumes were 2.25 cm^3 smaller (25%) at 31 GW [32]. Differences in segmentation protocol, gestational age estimation, anisotropic resolution, and motion between slices may explain the discrepancy in volume calculations.

Comparing to postnatal results from T1-weighted MRI studies [17, 18, 33] at equivalent gestational ages, cerebellar volume was on average 31% to 39% smaller between 27 and 31 GW. The lower volume calculations from the fetal MRI may be due to differences in image contrast, artifact introduced by image reconstruction, or variation in segmentation protocol.

Regardless of the absolute differences in volume, similar trajectories of growth were estimated from our data and previous studies of cerebellar development. 3D ultrasonography [14, 31] estimated an accelerating trajectory through 20 to 30 GW, as was shown in the present study. Further, a study of brain weight found that growth velocity of the infratentorial part of the brain (including the cerebellum) increased between 20 and 35 GW, after which the rate plateaued until term [4].

Though Limperopoulos et al. [17] conducted a linear regression from 27 to 44 GW in preterm neonates, which cannot address the question of acceleration, the study did show that the cerebellar percentage of total brain volume steadily increased over this age range. We observed a similar increase in the cerebellar ratio from 20 to 31 GW. This trend of more rapid relative cerebellar growth extends into the postnatal period when the cerebellum increases 240% over the first year, which is significantly greater than the cerebral volume increase of 100% [34]. By brain weight, the relative rate of cerebellar growth exceeds overall brain growth after 24GW [3, 4]. This corresponds to the peak proliferative phase of the external granular layer, which maintains its thickness from 25 to 40 GW [5]. Until term, growth of the cerebellum is dominated by the inward migration from the external to internal granular layers of the cortex, followed by outgrowth of fibers that make up the cerebellar cortical circuits. These cytoarchitectonic developments increase cerebellar cortical thickness and surface area expands exponentially [6]. In contrast, the cerebellar ventricular zone, source of deep nuclei and Purkinje cell precursors, is decreasing in thickness [5]. A comparable pattern is observed in the cerebral cortex of the same stages: After 25 GW, the ventricular zone is regressing, but progenitor cells in the subventricular zone continue to proliferate, providing another source of cortical precursors [35]. The subventricular zone,

particularly the outer layer [36], is more prominent in the primate and other gyroencephalic animals [37, 38] and is correlated with the emergence of cortical folding and accelerated cortical horizontal expansion [22, 39–41]. Therefore, while the cerebellar and cerebral cortices are both expanding rapidly, the cerebellar growth and ultimate cell number [3] exceed those of the larger cerebrum.

Curvature Reflects Gross Morphology of the Cerebellum

Qualitative study of the cerebellar morphology by in vivo [11] and ex vivo [42] MRI describes the increase in foliation, deepening of primary and emergence of secondary fissures in the second and third trimesters. Visual inspection of the cerebellum on MRI and segmentation-derived surface renderings (Fig. 6) clearly shows that the cerebellum transitions from a primarily dumbbell shape to an inverted heart. In this study, the temporal modeling of the local curvature of the outer cerebellar surface quantified where and in which direction the major changes were occurring.

For example, the curvature changes in the paravermian region correspond to the formation of the paravermian fissure. At 21 GW, the paravermian fissure is a shallow indentation [42]. Then as the hemispheres rapidly expand (shown by increasing convexity), the fissure deepens. This corresponds to the decreasing convexity around the inferior vermis and adjacent increasing convexity of the hemispheres.

Other changes in surface curvature appear to be due to the physical constraints of the surrounding tissue. For example, the decreased convexity along the roof of the fourth ventricle may be due to expansion of the vermal anterior lobe that is bounded by the adjacent brainstem. Similarly, the hemispheric growth is physically restricted. As the cerebellum grows, the hemispheres would "flatten out" against the rigid dural cavity and expanding occipital lobe. This is supported by the decreasing convexity of much of the superior and inferior hemispheric surfaces.

Future Applications

While the results shown here are based on manual segmentation, quantitative analysis would be enhanced by the development of a spatiotemporal atlas [43] for automated segmentation of the fetal brain [44] that included the cerebellum. Thus far, the cerebellum has been included in a spatiotemporal atlas of the premature and postnatal brain from 28 to 47 GW [33]. Addition of the cerebellum to the fetal spatiotemporal atlas will provide overlap with published postnatal studies and extension into earlier development.

Cerebellar malformation is a consequence of many developmental and genetic disorders [45], and cerebellar lesions are a risk in the premature period in part because the proliferative zones are in direct contact with CSF [6]. Application of the volumetric and morphometric methods used here to vulnerable populations may help quantify the severity of the insult and track potential growth and recovery.

Acknowledgments

References

1. Streeter, G. The development of the nervous system. In: Frenz, K.; Franklin, PM., editors. Manual of human embryology. Philadelphia: Lippincott; 1912. p. 1-116.

2. Larsell O. The development of the cerebellum in man in relation to its comparative anatomy. J Comp Neurol. 1947; 87(2):85–129. [PubMed: 20267600]

3. Dobbing J, Sands J. Quantitative growth and development of human brain. Arch Dis Child. 1973; 48(10):757–767. [PubMed: 4796010]

4. Guihard-Costa AM, Larroche JC. Growth velocity of some fetal parameters. I. Brain weight and brain dimensions. Biol Neonate. 1992; 62(5):309–316. [PubMed: 1467369]

5. Rakic P, Sidman RL. Histogenesis of cortical layers in human cerebellum, particularly the lamina dissecans. J Comp Neurol. 1970; 139(4):473–500. [PubMed: 4195699]

6. Volpe JJ. Cerebellum of the premature infant: rapidly developing, vulnerable, clinically important. J Child Neurol. 2009; 24(9):1085–1104. [PubMed: 19745085]

7. Sidman RL. Rakic Neuronal migration, with special reference to developing human brain: a review. Brain Res. 1973; 62(1):1–35. [PubMed: 4203033]

8. Laroche, JC. Developmental pathology of the neonate. Amsterdam: Excerpta Medica; 1977.

9. Larsell, O.; Jansen, J. The comparative anatomy and histology of the cerebellum: the human cerebellum, cerebellar connections, and cerebellar cortex. Minneapolis: University of Minnesota Press; 1972.

10. Adamsbaum C, Moutard ML, Andre C, Merzoug V, Ferey S, Quere MP, et al. MRI of the fetal posterior fossa. Pediatr Radiol. 2005; 35(2):124–140. [PubMed: 15565345]

11. Triulzi F, Parazzini C, Righini A. Magnetic resonance imaging of fetal cerebellar development. Cerebellum. 2006; 5(3):199–205. [PubMed: 16997751]

12. Vinals F, Munoz M, Naveas R, Shalper J, Giuliano A. The fetal cerebellar vermis: anatomy and biometric assessment using volume contrast imaging in the C-plane (VCI-C). Ultrasound Obstet Gynecol. 2005; 26(6):622–627. [PubMed: 16254881]

13. Sherer DM, Sokolovski M, Dalloul M, Pezzullo JC, Osho JA, Abulafia O. Nomograms of the axial fetal cerebellar hemisphere circumference and area throughout gestation. Ultrasound Obstet Gynecol. 2007; 29(1):32–37. [PubMed: 17171631]

14. Rutten MJ, Pistorius LR, Mulder EJH, Stoutenbeek P, de Vries LS, Visser GHA. Fetal cerebellar volume and symmetry on 3-D ultrasound: volume measurement with multiplanar and vocal techniques. Ultrasound Med Biol. 2009; 35(8):1284–1289. [PubMed: 19540660]

15. Hatab MR, Kamourieh SW, Twickler DM. MR volume of the fetal cerebellum in relation to growth. J Magn Reson Imaging. 2008; 27(4):840–845. [PubMed: 18302203]

16. Tilea B, Alberti C, Adamsbaum C, Armoogum P, Oury JF, Cabrol D, et al. Cerebral biometry in fetal magnetic resonance imaging: new reference data. Ultrasound Obstet Gynecol. 2009; 33(2):173–181. [PubMed: 19172662]

17. Limperopoulos C, Soul JS, Gauvreau K, Huppi PS, Warfield SK, Bassan H, et al. Late gestation cerebellar growth is rapid and impeded by premature birth. Pediatrics. 2005; 115(3):688–695. [PubMed: 15741373]

18. Tam EWY, Miller SP, Studholme C, Chau V, Glidden D, Poskitt KJ, et al. Differential effects of intraventricular hemorrhage and white matter injury on preterm cerebellar growth. J Pediatr. 2011; 158(3):366–371. [PubMed: 20961562]

19. Studholme C. Mapping fetal brain development in utero using magnetic resonance imaging: the big bang of brain mapping. Annu Rev Biomed Eng. 2011; 13(1):345–368. [PubMed: 21568716]

20. Scott JA, Habas PA, Kim K, Rajagopalan V, Hamzelou KS, Corbett-Detig JM, et al. Growth trajectories of the human fetal brain tissues estimated from 3D reconstructed in utero MRI. Int J Dev Neurosci. 2011; 29(5):529–536. [PubMed: 21530634]

21. Rajagopalan V, Scott JA, Habas PA, Kim K, Corbett-Detig JM, Rousseau F, et al. Local tissue growth patterns Cerebellum underlying normal fetal human brain gyrification quantified in utero. J Neurosci. 2011; 31(8):2878–2887. [PubMed: 21414909]

22. Habas PA, Scott JA, Roosta A, Rajagopalan V, Kim K, Rousseau F, et al. Early folding patterns and asymmetries of the normal human brain detected from in utero MRI. Cereb Cortex. 2012; 22(1):13–25. [PubMed: 21571694]

23. Messerschmidt A, Brugger PC, Boltshauser E, Zoder G, Sterniste W, Birnbacher R, et al. Disruption of cerebellar development: potential complication of extreme prematurity. AJNR Am J Neuroradiol. 2005; 26(7):1659–1667. [PubMed: 16091510]

24. Kim K, Habas PA, Rousseau F, Glenn OA, Barkovich AJ, Studholme C. Intersection based motion correction of multi-slice MRI for 3-D in utero fetal brain image formation. IEEE Trans Med Imaging. 2010; 29(1):146–158. [PubMed: 19744911]

25. Lopes A, Brodlie K. Improving the robustness and accuracy of the marching cubes algorithm for isosurfacing. IEEE Trans Vis Comput Graph. 2003; 9(1):16–29.

26. Do Carmo, M. Differential geometry of curves and surfaces. Englewood Cliffs: Prentice Hall; 1976.

27. Studholme C, Cardenas VA. A template free approach to volumetric spatial normalization of brain anatomy. Pattern Recognit Lett. 2004; 25(10):1191–1202.

28. Nichols TE, Holmes A. Nonparametric permutation tests for functional neuroimaging: a primer with examples. Hum Brain Mapp. 2002; 15(1):1–25. [PubMed: 11747097]

29. Garel C, Chantrel E, Elmaleh M, Brisse H, Sebag G. Fetal MRI: normal gestational landmarks for cerebral biometry, gyration and myelination. Childs Nerv Syst. 2003; 19(7–8):422–425. [PubMed: 12879340]

30. Reichel TF, Ramus RM, Caire JT, Hynan LS, Magee KP, Twickler DM. Fetal central nervous system biometry on MR imaging. AJR Am J Roentgenol. 2003; 180(4):1155–1158. [PubMed: 12646474]

31. Chang CH, Chang FM, Yu CH, Ko HC, Chen HY. Assessment of fetal cerebellar volume using three-dimensional ultrasound. Ultrasound Med Biol. 2000; 26(6):981–988. [PubMed: 10996698]

32. Grossman R, Hoffman C, Mardor Y, Biegon A. Quantitative MRI measurements of human fetal brain development in utero. Neuroimage. 2006; 33(2):463–470. [PubMed: 16938471]

33. Kuklisova-Murgasova M, Aljabar P, Srinivasan L, Counsell SJ, Doria V, Serag A, et al. A dynamic 4D probabilistic atlas of the developing brain. Neuroimage. 2011; 54(4):2750–2763. [PubMed: 20969966]

34. Knickmeyer RC, Gouttard S, Kang C, Evans D, Wilber K, Smith JK, et al. A structural MRI study of human brain development from birth to 2 years. J Neurosci. 2008; 28(47):12176–12182. [PubMed: 19020011]

35. Zecevic N, Chen Y, Filipovic R. Contributions of cortical subventricular zone to the development of the human cerebral cortex. J Comp Neurol. 2005; 491(2):109–122. [PubMed: 16127688]

36. Hansen DV, Lui JH, Parker PRL, Kriegstein AR. Neurogenic radial glia in the outer subventricular zone of human neocortex. Nature. 2010; 464(7288):554–561. [PubMed: 20154730]

37. Smart IHM, Dehay C, Giroud P, Berland M, Kennedy H. Unique morphological features of the proliferative zones and postmitotic compartments of the neural epithelium giving rise to striate and extrastriate cortex in the monkey. Cereb Cortex. 2002; 12(1):37–53. [PubMed: 11734531]

38. Reillo I, de Juan Romero C, Garcia-Cabezas MA, Borrell V. A role for intermediate radial glia in the tangential expansion of the mammalian cerebral cortex. Cereb Cortex. 2011; 21(7):1674–1694. [PubMed: 21127018]

39. Armstrong E, Schleicher A, Omran H, Curtis M, Zilles K. The ontogeny of human gyrification. Cereb Cortex. 1995; 5(1):56–63. [PubMed: 7719130]

40. Dubois J, Benders M, Cachia A, Lazeyras F, Leuchter RHV, Sizonenko SV, et al. Mapping the early cortical folding process in the preterm newborn brain. Cereb Cortex. 2008; 18(6):1444–1454. [PubMed: 17934189]

41. Clouchoux C, Kudelski D, Gholipour A, Warfield SK, Viseur S, Bouyssi-Kobar M, et al. Quantitative in vivo MRI measurement of cortical development in the fetus. Brain Struct Funct. in press.

42. Chong BW, Babcook CJ, Pang D, Ellis WG. A magnetic resonance template for normal cerebellar development in the human fetus. Neurosurgery. 1997; 41(4):924–929. [PubMed: 9316055]

43. Habas PA, Kim K, Corbett-Detig JM, Rousseau F, Glenn OA, Barkovich AJ, et al. A spatiotemporal atlas of MR intensity, tissue probability and shape of the fetal brain with application to segmentation. Neuroimage. 2010; 53(2):460–470. [PubMed: 20600970]

44. Habas PA, Kim K, Rousseau F, Glenn OA, Barkovich AJ, Studholme C. Atlas-based segmentation of developing tissues in the human brain with quantitative validation in young fetuses. Hum Brain Mapp. 2010; 31(9):1348–1358. [PubMed: 20108226]

45. Barkovich AJ, Millen KJ, Dobyn WB. A developmental and genetic classification for midbrain–hindbrain malformations. Brain. 2009; 132(12):3199–3230. [PubMed: 19933510]
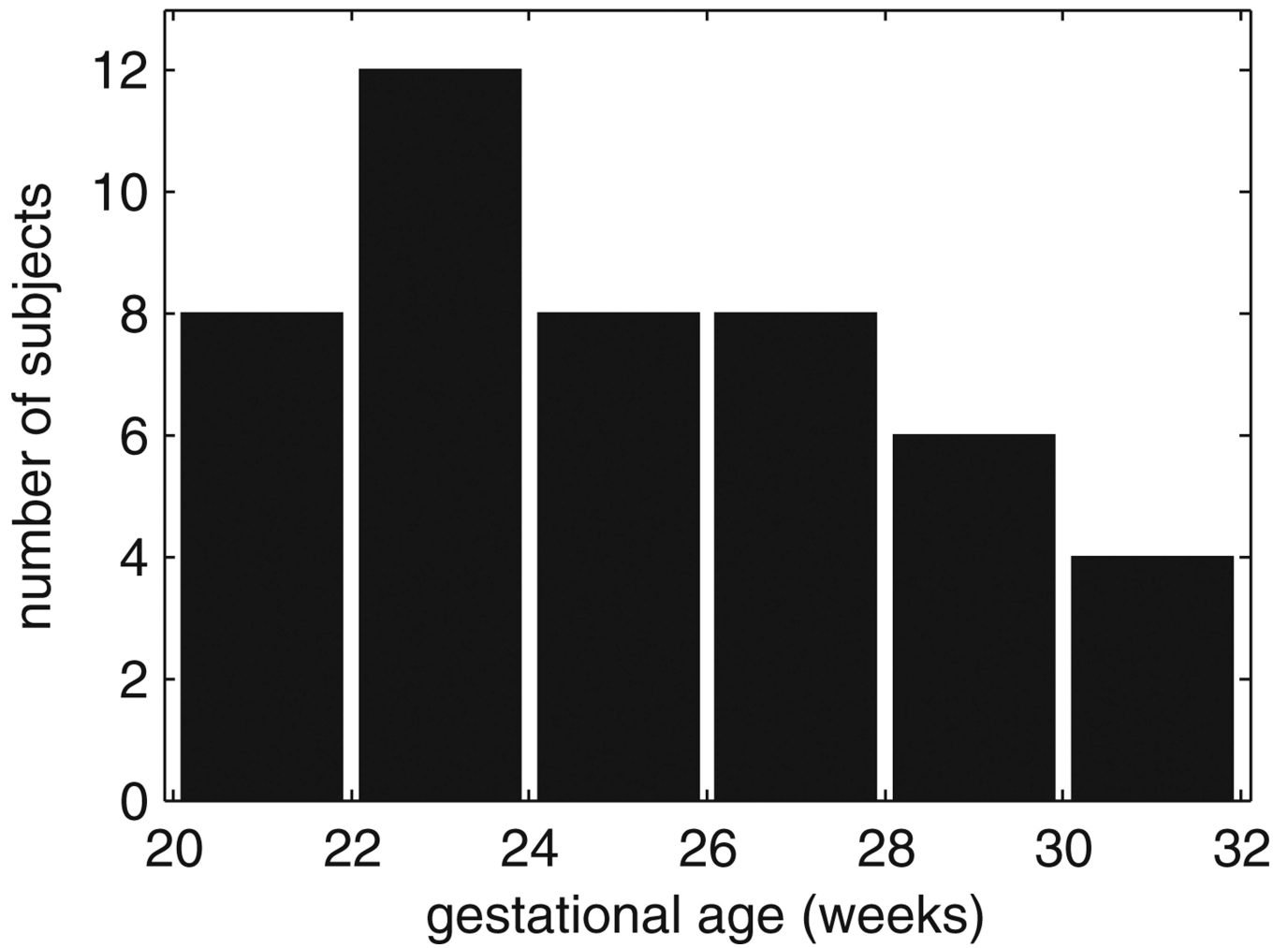
Fig. 1.
Histogram of the age distribution of fetal MR scans. All 2-week periods include at least four scans. Gestational age is calculated from last menstrual period
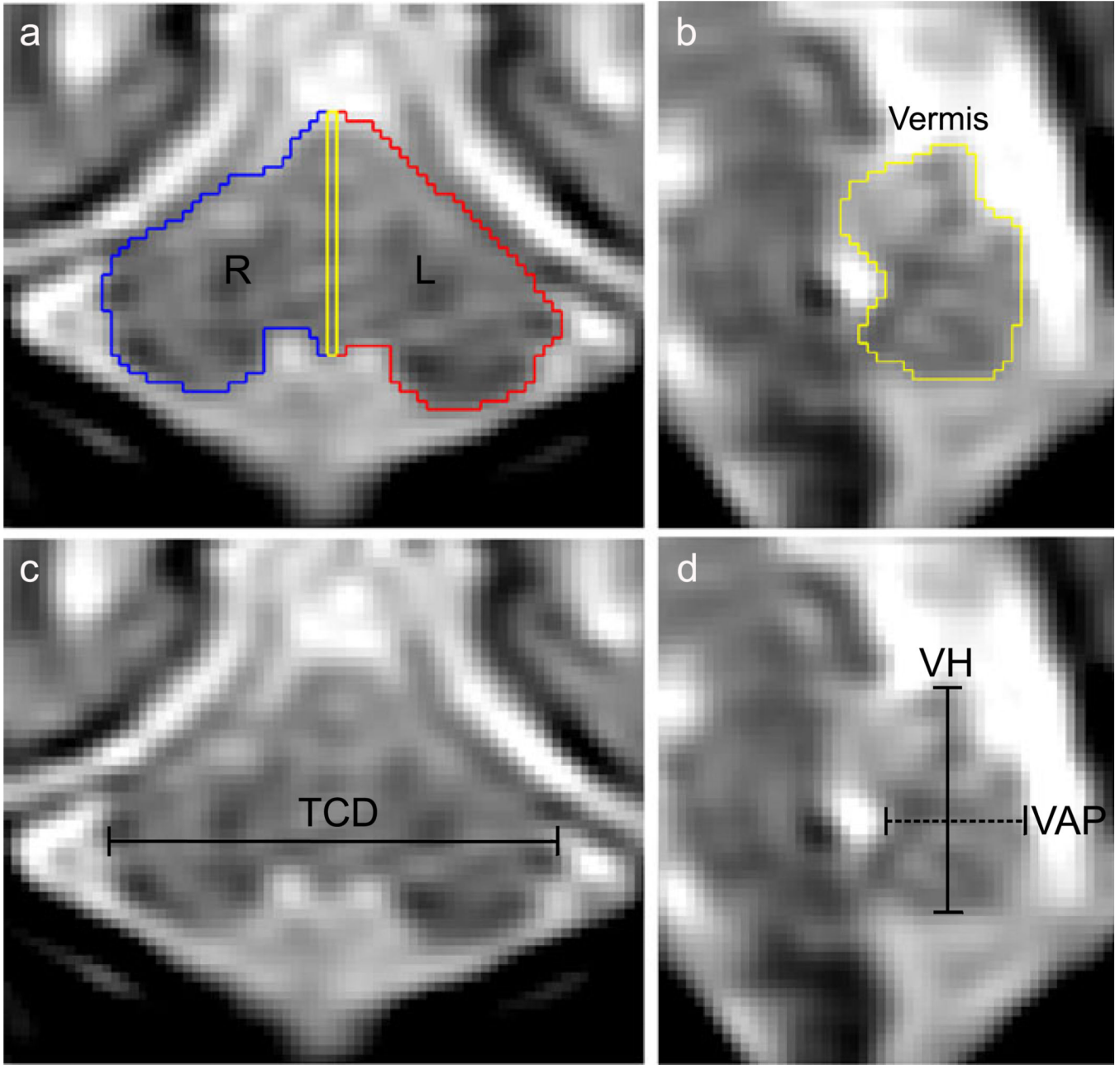
Fig. 2.
Example of cerebellum linear dimensions and volumetric segmentation at 25 gestational weeks. **a**, **b**) The perimeter of the cerebellum was manually drawn then labeled as right hemisphere (*blue*), left hemisphere (*red*), and midsagittal vermis (*yellow*). **c** Transverse cerebellar diameter (*TCD*) was measured at the maximum distance in the coronal plane. **d** Vermis height (*VH*; *solid line*) and anterior–posterior diameter (*VAP*; *dashed line*) were measured on the midsagittal slice Cerebellum
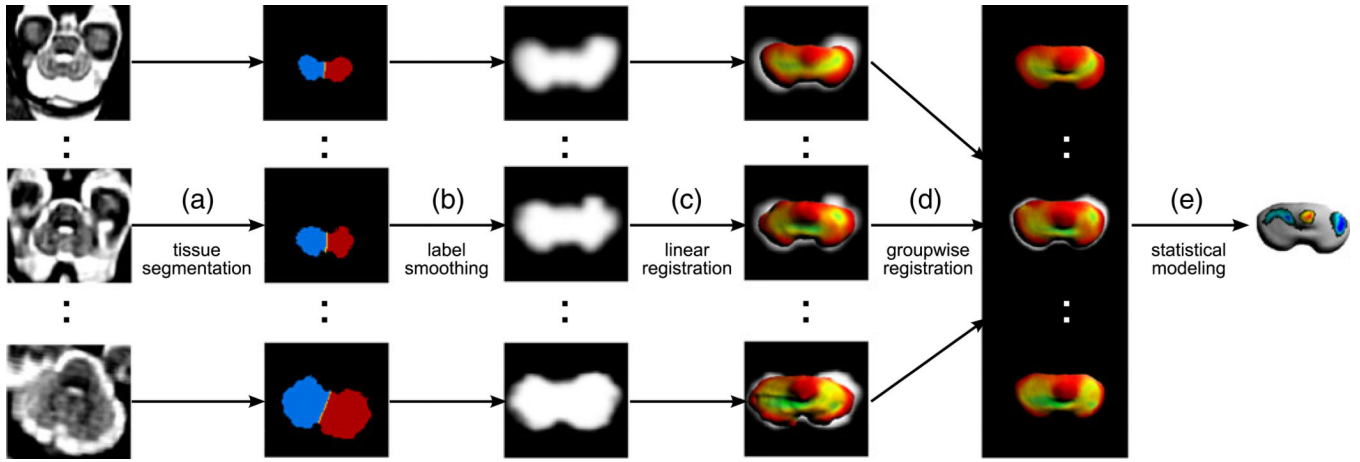
Fig. 3.
A dedicated image analysis framework for the mapping of cerebellar surface morphology from in utero MRI. *a* Motion-corrected 3D MRI volumes of the fetal brain are manually segmented into right and left cerebellar hemispheres and cerebellar vermis. *b* Tissue maps extracted from manual segmentations are smoothed with a Gaussian kernel. *c* To account for the overall brain growth, the maps are linearly registered to a reference anatomy and then tessellated into triangular meshes to reconstruct the outer surface of the fetal cerebellum. *d* Local measurements of mean surface curvature are mapped onto a population-average cerebellar surface established via volumetric group-wise registration. *e* Statistical modeling is performed for each vertex of the population-average surface to detect local patterns of curvature change Cerebellum
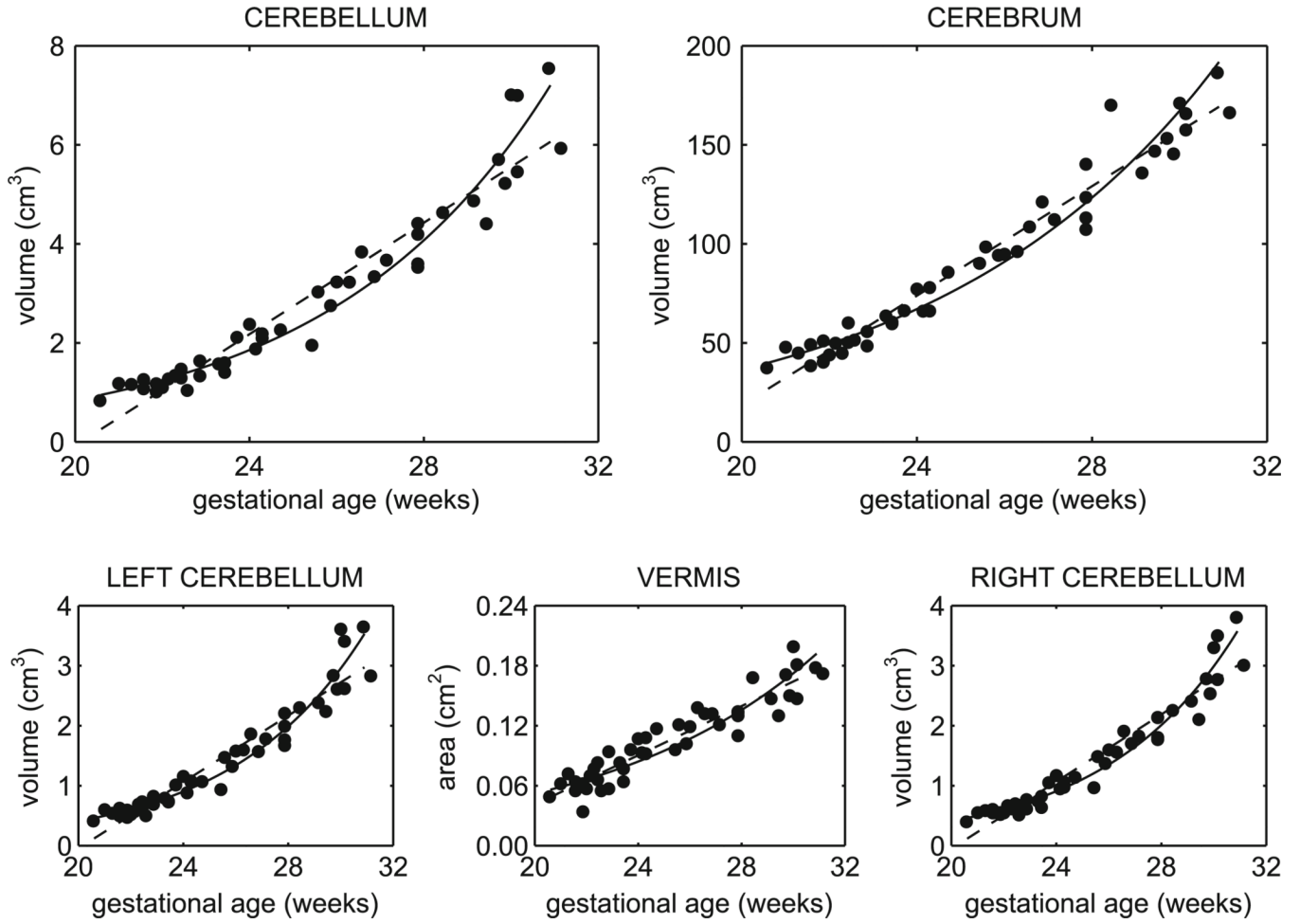
Fig. 4.
Linear and exponential growth curves for cerebral and cerebellar volumes from 20 to 31 GW. All structures significantly increased in volume and exponential trajectories better described the growth for the cerebellum (linear $R^2 = 0.92$, exponential $R^2 = 0.96$) and hemispheres, but not the midsagittal vermis (linear $R^2 = 0.88$, exponential $R^2 = 0.83$)
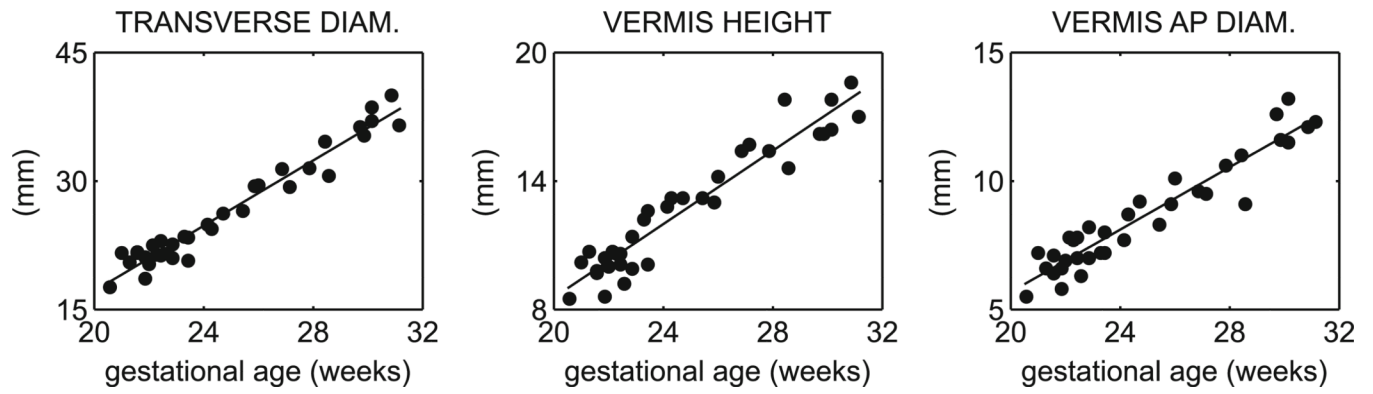
Fig. 5.
Linear dimensions of the cerebellum and vermis from 20 to 30 GW. The transverse cerebellar diameter ($R^2 = 0.95$), vermis height ($R^2 = 0.91$), and vermis anteroposterior diameter ($R^2 = 0.90$) significantly increased linearly
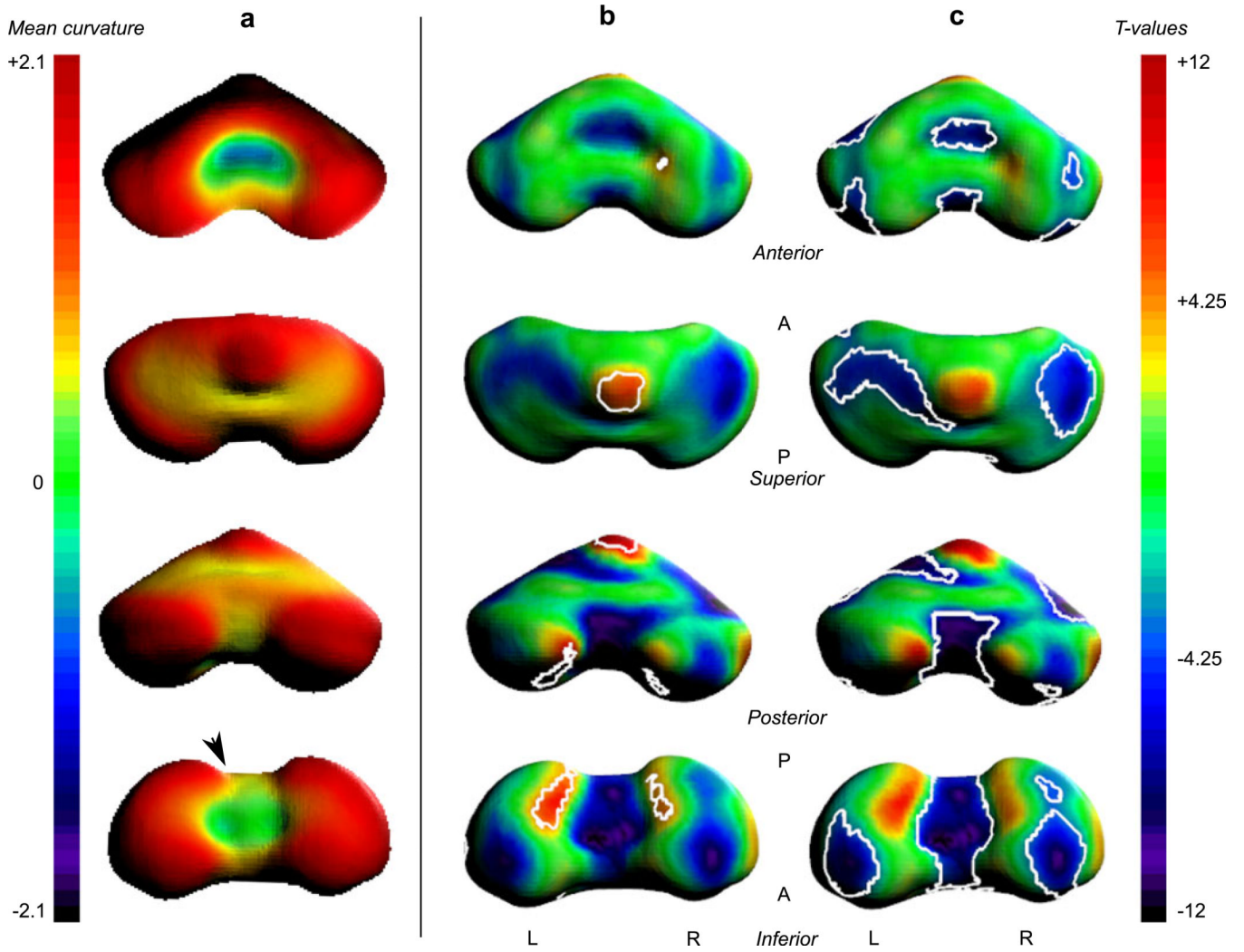
Fig. 6.
Local curvature analysis of the cerebellar surface. *a* The mean curvature across all ages is overlaid on the average surface. Positive values (*warm colors*) express local convexity, and negative values (*cool colors*) indicate local concavity. Age-related changes in local curvature were tested for significance with multiple comparisons correction at $p < 0.05$ ($|T| > 4.25$). The last two columns show the full *T* maps with contours around the significant increases (*b*) and decreases (*c*) in convexity. Changes in curvature surrounding the inferior vermis are related to the formation of the paravermian fissure (*arrow head*)

Table 1

Study demographics

Maternal participants	Number of		Maternal age (years)	Fetal age (GW)	
	Participants	Scans		At MRI	At Delivery
Total	40	46	19–41	20–31	37–42
Volunteer	23	27	23–41	20–31	37–42
Abnormal Ultrasound	10	12	29–39	21–30	38–42
Prior abnormal Pregnancy	7	7	19–39	21–24	38–41

Table 2

Temporal models of cerebellar growth

	R Hem	L Hem	Vermis	Cbl	TCD	VH	VAP
Linear ($y = b + at$)							
R^2	0.92	0.91	0.88	0.92	0.95	0.91	0.90
R^2_{adj}	0.92	0.91	0.88	0.92	0.95	0.91	0.90
Constant (b)	−5.6463	−5.5812	−0.2046	−11.3428	−20.9097	−8.5865	−6.4654
Growth rate (a)	cm³/week	cm³/week	cm²/week	cm³/week	mm/week	mm/week	mm/week
	0.2798	0.2768	0.0123	0.5633	1.9042	0.8575	0.6074
Quadratic ($y = b + at + ct^2$)							
R^2	0.95	0.94	0.88	0.95	0.96	0.92	0.90
R^2_{adj}	0.95	0.94	0.88	0.94	0.95	0.91	0.90
Constant (b)	7.0441	6.9762	−0.2494	13.8706	4.7666	−25.4269	−1.0294
Linear coefficient (a)	−0.7183	−0.7109	0.0158	−1.4198	−0.1195	2.1848	0.1790
Quadratic coefficient (c)	0.0193	0.0191	−0.0001	0.0384	0.0392	−0.0257	0.0083
Growth rate (a + 2ct)	cm³/week	cm³/week	cm²/week	cm³/week	mm/week	mm/week	mm/week
At $t = 22$ GW	0.1324	0.1309	0.0128	0.2704	1.6049	1.0537	0.5440
At $t = 26$ GW	0.2871	0.2840	0.0123	0.5777	1.9185	0.8481	0.6104
At $t = 30$ GW	0.4418	0.4370	0.0117	0.8850	2.2320	0.6425	0.6768
Exponential ($y = me^{nt}$)							
R^2	0.96	0.95	0.83	0.96	0.95	0.89	0.89
R^2_{adj}	0.96	0.95	0.82	0.96	0.95	0.88	0.88
Linear coefficient (m)	0.0078	0.0079	0.0048	0.0166	4.6612	2.4254	1.5689
Exponential coefficient (n)	0.1984	0.1975	0.1195	0.1965	0.0687	0.0657	0.0675
Growth rate (mne^{nt})	cm³/week	cm³/week	cm²/week	cm³/week	mm/week	mm/week	mm/week
At $t = 22$ GW	0.1213	0.1203	0.0079	0.2463	1.4525	0.6752	0.4675
At $t = 26$ GW	0.2683	0.2649	0.0128	0.5405	1.9120	0.8781	0.6123
At $t = 30$ GW	0.5934	0.5836	0.0206	1.1863	2.5169	1.1418	0.8021

All models fit significantly ($p < 0.001$)